POLYMODE NEWS

No. 72 November 16, 1979

In this issue:

XBT ACCURACY

by George Seaver and Stanislav Kuleshov

During the November-December 1977 POLYMODE cruises of the Mikhail Lomonosov, 103 XBT-STD (Istok) and 14 XBT-XBT comparisons were made. The results were qualitatively similar to previous studies, and they greatly improve the existing statistics of the XBT mean and random errors.

Figure 1 shows the mean error and the standard deviation (σ) of the random error along with the results of previous experiments (Flierl and Robinson, 1977; McDowell, POLYMODE News No. 29; Fedorov et al., POLYMODE News No. 50). Survey 8 (November 1977) and Survey 9 (December 1977) differ by a nearly constant six-meter offset in depth, which is probably due to a pressure error in the STD during Survey 8. Also, Survey 9 is a smoother curve. All of the results exhibit a positive excursion (negative curvature) in the 18° water, the region of small mean temperature gradient. Finally, all of the results show positive curvature as the main thermocline is approached with two of the mean curves having zero slope here. These properties will be important later in regards to the analytical models of the error. The random error of Survey 9 exhibits a deeper and weaker minimum near 100 m, reflecting the deeper and weaker seasonal thermocline during December. The remaining portions of the σ curves are quite similar with Survey 8 being somewhat larger and noisier.

Also plotted is the standard deviation for the 14 XBT-XBT comparisons, a subset of Survey 8. The results are somewhat smaller than the XBT-STD results, the difference representing the noise introduced by using the STD to determine the mean. Also shown is the standard deviation from McDowell of the strip chart recorder-Bathy Systems Digitizer (SCR-BSD) comparison. These data are for a different recorder and mean temperature gradient and probably are different quantitatively from what it would be for the present study. However, it indicates that significant random noise exists in the analog recorder and manual digitizing process (McDowell, POLYMODE News No. 58). Table 1 summarizes the contributions to the random error by the STD and the strip chart recorder. Although the standard deviations (σ) for the XBT vs. XBT and SCR vs. BSD are for different water columns, we believe Table 1 is a useful demonstration of what is involved.

The calculation for σ is quadratic and the total random error is not a simple sum of its parts. However, it is clear from Table 1 that a major part of the random error is from the STD comparison and the XBT recorder procedures. Further, Figure 2 shows temperature vs. depth profiles for two XBTs taken in the same location one hour apart, at the beginning and the end of an STD drop. The Brunt-Väisälä frequency has

(continued page 5)

NOTES from the Editor

You may have noticed that the amount of material in POLYMODE News is dropping off. The size of the issues has not been significantly reduced, but the frequency of issuance is decreasing. Rather than simply cease in the near future we will continue to issue the News for some time longer, since we have been informed that some worthwhile contributions are still being prepared and will be sent to us for inclusion.

If you anticipate having any material for POLYMODE News, please get in touch with Catherine Herrity so that she can make plans accordingly. Judging from what we have been told about articles in the works, the News will likely expire, due to lack of material, sometime in the first half of 1980.

- - - - - - - - - - - - - - -

Data from the Bermuda Biological Station tide gauge from 1932 through 1979 can now be obtained from: Associate Director, Office of Oceanography, C2, National Ocean Survey/NOAA, 6001 Executive Blvd, Rockville MD 20852. Historical data are summarized in the form of monthly and yearly means of tidal datums, i.e., mean low and mean high water and mean sea level, and extreme water levels. For recent years, times and heights of high and low waters and hourly heights can be provided.

--F. W.

The POLYMODE* News is produced at the Woods Hole Oceanographic Institution. It is edited by Ferris Webster and Catherine Herrity.

Material of interest for this newsletter may be sent to Catherine Herrity at the Woods Hole Oceanographic Institution, Woods Hole, MA, 02543, Telephone (617) 548-1400, ext. 2550, TWX 710-346-6601; or to Ferris Webster at NOAA/RD, 6010 Executive Blvd, Rockville, MD, 20852, Telephone (301) 443-8344.

*POLYMODE is derived from the names of the USSR POLYGON experiments and the Mid-Ocean Dynamics Experiment (MODE).

CONTRIBUTORS

Mr. Stanislav Kuleshov
Marine Hydrophysical Institute
Lenin Str, 28
USSR Sevastopol 335000

Dr. George Seaver
Aero Management Associates
Hyannis MA 02601
(617) 771-8273

Dr. Colin Shen
Department of Oceanography WB-10
University of Washington
Seattle WA 98195
(206) 543-5129

ERRATUM

Seaver (POLYMODE News No. 64)

A line was inadvertently omitted from the second paragraph of Seaver's article entitled "Surface currents in the POLYMODE XBT area." Line 12 in paragraph 2 should read "Loran A was not useful at night. The ship's speed was 10.2 knots (±0.2 knots) and the ship's course on automatic pilot was generally good to 1°."

ACKNOWLEDGEMENT

The POLYMODE News is produced with support from the International Decade of Ocean Exploration (IDOE) of the National Science Foundation, the Office of Naval Research, and the National Oceanic and Atmospheric Administration.

AN EXAMPLE OF THE LAGRANGIAN MASS TRANSPORT BY FINITE AMPLITUDE ROSSBY WAVES

by Colin Shen

The Lagrangian fluid motion (Stokes drift) is principally responsible for the mass transport in a wave field of infinitesimal amplitude. Whether this applies to nonlinear, finite-amplitude waves is a question of considerable interest. This is especially so in the study of mass transport by finite-amplitude Rossby waves since this question bears directly upon the advection of water properties by mesoscale eddies in the ocean.

An example of Lagrangian transport by finite-amplitude Rossby waves will be presented to demonstrate its possible importance. In the example, we use a wave field composed of non-interacting Rossby waves. This wave field satisfies the potential vorticity equation, and its Lagrangian solution can be computed exactly. The main result to be shown in this note is that at a sufficiently high amplitude, some of the fluid masses are trapped and carried westward by the wave field at the wave's phase speed, while the rest of the masses are advected by the wave field at a large speed to the east. In the limit of small amplitude the result reduces simply to that of Stokes drift. The present finding may have some implications concerning the mass transport by mesoscale eddies. However, the existence of such transport in a more general wave field remains to be seen and is under investigation.

For the following, it is sufficient to consider the wave motion in a constant depth, homogeneous fluid on a beta-plane. In this fluid, the potential vorticity equation is then given by

$$[\frac{\partial}{\partial t} + J(\psi)](\nabla^2\psi + \beta y) = 0 \qquad (1)$$

where ψ is the usual streamfunction whose first derivatives, $\partial\psi/\partial x = v$ and $-\partial\psi/\partial y = u$, are respectively the north and the east component of the velocity. The non-interacting waves which satisfy (1) are those having equal westward phase speed or, equivalently, equal magnitude wave number vector.

A convenient form of the wave field to work with here is

$$\psi = (\psi_o/2) \sum_i \sin[\kappa_i(x+c_x t)+\ell_i y], \quad i = 1,2 \qquad (2)$$

which is composed of two non-interacting Rossby waves denoted by the suffix i = 1,2, with each having the same westward phase speed $c_x = \beta/(\kappa_i^2 + \ell_i^2)$.

We now show that the wave field given by (2) can produce "particle" speed greater than or equal to the phase speed at a sufficiently high amplitude ψ_o, thereby demonstrating that the wave carries the mass directly. In order to show this, one normally needs to determine the fluid particle speed and hence the Lagrangian motion, which is generally a difficult task. For a simple wave field as (2), however, it is sufficient to compute the Eulerian velocity and show the existence of the following

$$\frac{\partial\psi}{\partial y} = c_x , \quad \frac{\partial\psi}{\partial x} = c_y = 0 , \qquad (3)$$

i.e., the instantaneous Eulerian speed equals the phase speed.

As will be seen shortly, where (3) is satisfied the fluid also preserves its potential vorticity. Since a fluid particle conserves its own potential vorticity, (3) also implies that the particle speed equals the phase speed. Given (2) and (3), the calculation is now straightforward. Rewriting (2) as

$$\psi = \psi_o \sin[K_1(x+c_x t)+L_1 y]\cos[K_2(x+c_x t)+L_2 y] \qquad (4)$$

with $K_1 = (\kappa_1+\kappa_2/2), L_1 = (\ell_1+\ell_2)/2$

and $K_2 = (\kappa_1-\kappa_2)/2$, $L_2 = (\ell_1-\ell_2)/2$,

condition (3) becomes

$$\begin{aligned} L_1\cos\phi_1\cos\phi_2 - L_2\sin\phi_1\sin\phi_2 &= c_x/\psi_o \\ K_1\cos\phi_1\cos\phi_2 - K_2\sin\phi_1\sin\phi_2 &= 0 \end{aligned} \qquad (5)$$

where ϕ_1 and ϕ_2 denote the phase functions of sin and cos in (4), respectively. Equation (5) may be solved alternately for sin and cos, and one has

$$\begin{aligned} \cos\phi_1\cos\phi_2 &= (K_2 c_x)/(\psi_o D) \\ \sin\phi_1\sin\phi_2 &= (K_1 c_x)/(\psi_o D) \end{aligned} \qquad (6)$$

with $D = K_2L_1 - K_1L_2$. The ratio of the above two equations gives

$$\tan\phi_1\tan\phi_2 = K_1/K_2. \qquad (7)$$

This condition determines the instantaneous position of the particle that satisfies (3). Given a pair of K_1 and K_2, there is always a solution to (7); in fact, infinitely many.

(continued page 4)

AN EXAMPLE OF THE LAGRANGIAN MASS TRANSPORT BY FINITE AMPLITUDE ROSSBY WAVES (continued)

The appropriate root, however, is determined by the wave amplitude condition

$$\psi_o = (K_1 c_x)/(D \sin\phi_1 \sin\phi_2) = (K_2 c_x)/(D \cos\phi_1 \cos\phi_2). \quad (8)$$

Clearly, for a sufficiently large ψ_o ($>K_1 c_x/D$ or $K_2 c_x/D$), a unique solution to (7) can be found and (3) exists. The exception to the above is the case D = 0. Here, all constant phase lines given by (2) are parallel and all particle motions are normal to the direction of the phase propagation; thus, (3) cannot be satisfied. A single Rossby wave will not satisfy (3) for the same reason. The potential vorticity for the wave field (2) has the form

$$\nabla^2\psi + \beta y = (-\beta/c_x)\psi + \beta y . \quad (9)$$

It can be readily shown that the extremum of the potential vorticity is also given by (3). Thus, the instantaneous position of the potential vorticity extremum and the position where the fluid motion equals the phase speed are the same. This shows that the positions given by (7) and (8) are also the particle positions. It can be concluded that the particles there move with the wave at the same speed. Finally, it should be pointed out that in a reference frame moving with the wave, the positions given by (7) and (8) are stationary.

Figures 6 and 7 illustrate the patterns of the streamlines of (2) and also the corresponding potential vorticity field for two different orientations of the constant phase lines. The patterns in all these figures move to the west (left edge) without changing shape. Since the potential vorticity is conserved with respect to the fluid particle, each of the constant potential vorticity lines in Figures 6b and 7b represents the path of the particles. Thus, the closed contour lines indicate that the particles are trapped and move westward with the wave at the same speed.

The circulation within the trapped region in Figure 6b resembles that of "modon" with anticyclonic circulation in the upper half -- since the potential vorticity there is less than the background, βy, planetary vorticity. The motion is cyclonic in the lower half.

The trapped regions in Figure 7b artificially resemble planetary "solitons." The sense of the circulation within each is easily deduced from the background planetary vorticity. Outside of the trapped region in both figures, the direction of the mass transport is to the east. This is obvious since the mass must be conserved. By knowing the particles' paths which are the isopotential vorticity lines, one is, in principle, in a position to compute the speed of the Lagrangian particle motions. We shall refrain from presenting a detailed discussion here. Instead, we consider a special case below ($K_2 = 0 = L_1$) to illustrate the connection between the mass transport discussed in this note and the Stokes drift.

In this case the amplitude condition (8) for the existence of trapped mass becomes $\psi_o = -c_x/(L_2 \sin\phi_1 \sin\phi_2)$, which implies that the amplitude be at least $|\psi_o| = c_x/L_2$. For the moment, we assume that the amplitude is small, $c_x >> \psi_o L_2$, and compute the Stokes drift of the wave field. This is easily done by means of Stokes' expansion, and the result after averaging over a wave cycle is

$$U_S = (\psi_o^2 L_2^2/2c_x) \cos 2L_2 y. \quad (10)$$

The drift is maximum and westward at $y = \frac{\pm\pi}{2L_2}$, and is eastward at y = 0 (see Figure 8). The above formula is not valid for $\psi_o L_2 \lesssim c_x$. In this range, the wave amplitude is finite, and a different approach is required to determine the Lagrangian particle motion. As stated above, the particle always moves along a constant potential vorticity line. This fact suggests a convenient method of calculation.

First, note that along a constant potential vorticity line (call it a constant Q line) the Lagrangian velocity, $\underset{\sim}{U}$, is given by

$$\underset{\sim}{U}(\underset{\sim}{x}_o, t) = \underset{\sim}{u}(x,y,t) = \underset{\sim}{u}[x, y(x,t,Q), t], \quad (11)$$

where $\underset{\sim}{u}$ is the Eulerian velocity and $\underset{\sim}{x}_o$ is the initial position of the Lagrangian particle (serving as a "tag"). The last term in (11) follows because x and y are related by Q(x,y,t) = constant. The rate of the displacement of the particle is as usual $d\underset{\sim}{x}/dt = \underset{\sim}{U}(\underset{\sim}{x}_o, t)$. With (11), the rate of displacement can be

$$d\underset{\sim}{x}/dt = \underset{\sim}{u}[x, y(x,t,Q), t]. \quad (12)$$

This is a first-order, ordinary differential equation. Since $\underset{\sim}{u}$ is known the equation can be solved, and the displacement of the

(continued page 9, lower half)

XBT ACCURACY (continued)

a period from 1.2 minutes in the seasonal thermocline to 10 minutes in the 18° water. Consequently, internal waves could be responsible for the differences between the two temperature profiles. The coincident points down the profile rule out the usual instrument problems. At 70 m depth a 4 m depth difference translates into a 1.1°C temperature "random" error. For the 18.3°C isotherm, a 0.15°C temperature difference between the two profiles translates into a 35 m random depth error. During Survey 8, the mixed layer varied from 15 m to 85 m with winds of 25 knots for two-day periods. The forcing for internal waves is available. From the above considerations, the random error contribution of the XBT probe itself is probably a small part of the total random error observed by at-sea experiments.

The various experimental mean errors of Figure 1 are difficult to interpret without a dynamical model. An at-sea calibration of the XBT against the STD is valid for the probe type used and the temperature profile in the region of comparison. A correct dynamical model of the error would generalize the results to all temperature profiles and probe types (reference temperature).

From Figure 3a, the kinematic viscosity changes by 42% between 10°C and 25°C; the possibility that decreasing temperature with ocean depth significantly changes the XBT probe fall rate is explored below. Figure 3b is a composite from Schlichting showing the terminal velocity of streamlined bodies as a function of viscosity. The slope of the curve is of interest here; the vertical position of the curve segments is not necessarily correct. Also, the Reynolds number (Re. No.) as indicated in Figure 3b denotes its approximate value of transition between the various regimes and not a functional dependence. The Reynolds number of the XBT probe based upon its diameter is 3.5×10^5. The probe is in transition between a laminar and a turbulent boundary layer. From Schlichting (1955) the boundary layer drag (d) on a streamlined body is:

$$d = \text{constant}\ \rho\ U^2\ \left(\frac{UL}{\nu}\right)^{-\frac{1}{n}} \qquad (1)$$

$$U[\nu(T)] = \text{constant}\ \nu^{-\frac{1}{2n-1}} \qquad (2)$$

$$\Delta U = \left(\frac{\Delta U}{\Delta \nu}\frac{1}{U}\right) U\Delta\nu = -\frac{1}{2n-1}\,\nu^{-1}\,U\Delta\nu \qquad (3)$$

$$\Delta U = \frac{\nu^{-1}}{2n-1}\frac{\Delta\nu}{\Delta T}\frac{\Delta T}{\Delta D}\,U^2\,\Delta t \qquad (4)$$

$$\Delta D = \int \Delta U\ \Delta t \qquad (5)$$

where:

U = XBT fall rate (terminal velocity) ≐ 6.5 m/sec

ν = kinematic viscosity

T = temperature

D = depth

tc = thermocline

t_{ref} = time of arrival to reference temperature and depth at 6.5 m/sec

n = 2 for laminar, 5 for turbulent case (Schlichting, 1955)

t = time

ΔD = XBT systematic error

T_{ref} = XBT probe calibration temperature

ml = mixed layer

18 = 18° water

Equation (4) is valid for small changes in the variables (an exact analysis is left to the computer); the results presented here are good to first order. The mean temperature profile has been broken into three straight line segments: the mixed layer to 100 m; the 18° water to 500 m; and the main thermocline. The zero-order fall rate used is 6.5 m/sec, the value Sippican Corporation (Marion MA) uses for their depth determination. Sippican does not know the calibration velocity and temperature to the required accuracy. Consequently, the fall rate calibration temperature (chart drive RPM and chart paper grid size) has been taken at 11°C (52°F at 750 m). From Figure 1, this is where the boundary condition $\frac{\partial \Delta D}{\partial t}$ (the fall rate error) is closest to zero. Equation (5) becomes:

$$\text{laminar}\ \Delta D = -.699t - .378(t-t_{18}) - .0066\left[t_{ref}(t-t_{tc}) - \frac{1}{2}(t^2-t^2_{tc})\right], \qquad (6)$$

$$\text{turbulent}\ \Delta D = -.233t - .126(t-t_{18}) - .0022\left[t_{ref}(t-t_{tc}) - \frac{1}{2}(t^2-t^2_{tc})\right]. \qquad (7)$$

The laminar case has a maximum error of 30 m, which is excessive. The turbulent case is presented in Figure 4, and has a smaller maximum error than the experimental results. As pointed out previously, the Reynolds number of the probe is 3.5×10^5,

(continued page 6)

and the boundary layer is partly laminar and partly turbulent. The point of transition to turbulence is probably at the point of inflection in the probe's shape (near the end of the zinc portion). This is where the Reynolds number based upon the boundary length is 3.5×10^5; this is also where an adverse pressure gradient develops. The slope of the terminal velocity-viscosity curve is then obtained by weighting the slopes of the laminar and turbulent cases of equations (6) and (7) in proportion to the probe surface areas of the two regimes (Schlichting, 1955). The slope then becomes

$$m = \frac{\Delta U}{\Delta \nu} = -0.173 \frac{\Delta \nu}{\nu} U$$

The results are plotted in Figure 4 and show better agreement. This will be discussed later.

Ballast and rereeling errors have been investigated. Rearranging equation (1):

$$U(m) = [m_0 \; g \; (1-t/t_0)]^{.586} \text{ x constant} \qquad (1)$$

$$D \doteq \text{constant } (t-.293 \; t^2/t_0) \text{ for } t^2/t^2{}_0 << 1$$

where

m_0 = initial total mass.

t_0 = XBT fall time/ratio of wire to total weight.

Sippican corrects for the loss of weight and drag from dereeling with an empirical relation:

$$D = At(1 - Bt)$$

The error in the correction of the above equation is

$$\Delta D = 6.472 \; (\frac{.293}{t_0} - .000334)t^2; \quad 750 \text{ m, T-7 probe} \qquad (8)$$

$$\Delta D = 6.828 \; (\frac{.293}{t_0} - .000267)t^2; \quad 1800 \text{ m, T-5 probe} \qquad (9)$$

The results are presented in Figure 4. They show poor agreement with experiment (error of the wrong sign) for a wire weight of 15% as specified by Sippican. There is much better agreement for a hypothetical wire weight of 5%, although it is difficult to believe that the probe or wire weight could be off by 75 grams. Conversely, the empirical and theoretical fall-rate relations agree to 2.2 m at 750 m for the design wire weight ratio providing some confidence in the theory. Below 650 m, the hypothetical dereeling results begin to diverge from experiment; it increases quadratically with depth.

As all of the experimental results show a positive hump in the mean error curve for small mean temperature gradient, a small positive temperature axis error is suggested. This is supported by Georgi et al. (POLYMODE News No. 71). Sippican corrects for the non-linearity of the thermistor temperature-resistance relation with a fourth-order polynomial accurate to 0.025°C. From these considerations a +0.025°C temperature axis error has been assumed. This is multiplied by the inverse of the mean temperature gradient to obtain the equivalent depth error, and is plotted in Figure 4. The mean error from Survey 9 has been corrected for this temperature axis error in Figure 4; the resultant mean error is in better agreement with the fall rate theory and a more reasonable function of depth. The full equation for the mean theoretical XBT error is

$$\overline{\Delta D} = \Delta U_{ml} \; t = \Delta U_{18} \; (t-t_{18}) + A_{tc}[t_{ref}(t-t_{tc}) - \tfrac{1}{2}(t^2-t^2{}_{tc})] - .025 \; [\frac{\overline{\Delta T}}{\Delta Z}]^{-1} + B_{dr} \; t^2 + \Delta U_{Ballast} \; t. \qquad (10)$$

The first three terms are the temperature-viscosity-drag effect; this contribution has a positive curvature. The fourth term is the temperature axis error and exhibits a positive hump in the 18° and 4° water where the mean temperature gradient is small. The fifth term is the dereeling effect; it has a quadratically increasing value, positively or negatively. The sixth term is the ballast error effect; it has a constant plus or minus slope.

From the above properties the temperature-viscosity effect would be the major contributor to the systematic XBT error.

Figure 5 shows the depth error vs. depth for the 1800 m, T-5 probe from McDowell (POLYMODE News No. 29). The T-5 probe has a different shape than the T-7 with an extended mid-section, greater weight, and a somewhat faster design fall rate. The viscosity-drag theory gives the change in fall rate, not the absolute fall rate.

(continued page 7)

XBT ACCURACY (continued)

Consequently, it is as applicable to the T-5 probe as it is to the T-7 probe. The boundary condition, $\frac{\partial \Delta D}{\partial t} = 0$, is taken at 100 m. The probe enters the water on average with nearly the design velocity, as shown by Figure 5. For the T-7 probe it was previously suggested that the XBT error is: $\overline{\Delta D} = f(T-T_{ref}, t, \overline{\Delta T}/\overline{\Delta Z})$, where the value of T_{ref} depends on the probe type. In the case of the T-7 probe, $(T-T_{ref})>0$ and $\overline{\Delta D}<0$. Now, for the T-5 probe, $(T-T_{ref})<0$ and the mean XBT error is positive.

As before, the experimental mean exhibits a positive curvature in the main thermocline (500-1100 m), and positive humps in the 18° and 5° water. An implied +.025°C temperature axis error results in a single-valued error curve and improved agreement between the fall-rate theory and experiment. A dereeling correction error is also shown in Figure 5 and shows poor agreement with the experimental error for the design wire weight ratio of 28.4%; conversely, the empirical and theoretical fall rate relations agree to 11 m at 1830 m depth for the design wire weight. This encourages belief in the functional relation of the theory. A hypothetical wire weight ratio of 38% is shown and is in much better agreement with experiment, although it is difficult to believe that the probe or wire weight could be off by 90 grams, as Sippican's weight specifications are to ±0.36%. The 95% confidence limits on the experimental mean are ±5.1 m at 1600 m depth, and include the temperature-viscosity theory. Finally, the temperature-viscosity explanation of the XBT systematic error appears valid from the results of the T-5 and T-7 probes.

A depth error from fall-rate variations would be a monotonically increasing function of time and depth from equation (10). The T-7 probe results show a 6.0 m increase in σ between the seasonal and main thermocline from Table 1. From this it is seen that fall-rate variations are an important part of the resultant random error. Table 2 summarizes the potential random errors derived from equation (10) of varying probe roughness (laminar-turbulent or all turbulent boundary layers), varying probe weights, and a 0.025°C thermistor variability. These points will be discussed in detail in a future

(continued page 9, upper half)

Comparison		T-7 Probe: Seasonal Thermocline	T-7 Probe: 18° Water	T-7 Probe: 750 m
I.	XBT vs. STD:			
	$\sigma(\Delta D')$	5.5 m	14 m	9.75 m
	$\sigma(\Delta T')$	0.35°C	0.09°C	0.25°C
II.	XBT vs. XBT:			
	$\sigma(\Delta D')$	3.0 m	12.5 m	8.50 m
	$\sigma(\Delta T')$	0.34°C	0.040°C	0.19°C
III.	Strip Chart Recorder vs. Bathy Systems Digitizer:			
	$\sigma(\Delta D')$	2.0 m	8.5 m	1.50 m
	$\sigma(\Delta T')$	0.07°C	0.025°C	0.034°C
	$\sigma_{II}(\Delta D')-\sigma_{III}(\Delta D')$	1.0 m	4.0 m	7.00 m
	$\sigma_{II}(\Delta T')-\sigma_{III}(\Delta T')$	0.27°C	0.015°C	0.15°C

Contributions to the random error by the strip chart recorder and STD.

Table 1 (Seaver and Kuleshov)

THEORY				
Cause	Depth, Maximum Error	Temperature, Maximum Error	Maximum $\sigma(\Delta D')$	Remedy
Probe nose roughness	7.0 m at 700 m		4.6 m	Trip boundary layer at nose front
Probe nose/ wire wt. 0.36% variations 2.0%	1.6 m 8.8 m at 750 m		1.1 m 6.2 m	Quality control and random weight checks
Non-vertical trajectories	-		-	Design of probe shape; rotation
Thermistor variability	5 m (18° water)	.025°C	3.5 m	Note thermistor batch number and calibration from manufacturer
	25 m (4° water)	.025°C	17.7 m	

$$\sigma_{max} = \left[\frac{2N(\Delta D')^2}{N}\right]^{\frac{1}{2}}$$

XBT probe random errors.
Table 2 (Seaver and Kuleshov)

Variable	Improvement	Accuracy
Depth	Define, remove systematic error. Reduce random error.	4 m at 800 m 0.5%
Temperature	Record thermistor calibration. Provide digital interface to XBT recorder.	.025°C
Salinity	θ-S relation -- MODE area.	.02°/$_{oo}$
	XSBT	?
Dynamic height	Using the θ-S relation (POLYMODE area) between 100 and 800 db.	8%
	Between 500 and 1500 db: 3.9 db in depth, .0067°/$_{oo}$ salinity, and .029°C.	5% 0.5 cm

Dynamic height accuracy of XBT probes.
Table 3 (Seaver and Kuleshov)

XBT ACCURACY (continued)

paper by Seaver and Kuleshov entitled "Experimental and theoretical XBT error."

A comment is necessary on the mixed-layer. Between winter and summer in the POLYMODE area the mixed layer temperature changes by 6°C. From equation (3) this represents a change in fall rate of 0.126 m/sec, or a displacement of the theoretical error curve of 1.9 m from summer to winter, and could explain the variability between the experimental results of Figure 1 above 200 m. This introduces the thought of a "Mathews Tables" type of correction (geography and season) for fall rate and depth, similar to the correction for sound velocity and depth in echo sounding.

Finally, the XBTs' potential accuracy in oceanography is summarized in Table 3. If the XBT systematic error were confirmed and removed and the random error reduced, its error in depth could be reduced to ∿4 m or 0.5%, the 95% confidence limits on the mean experimental error. There is evidence (Georgi et al., POLYMODE News No. 71) that by noting the thermistor batch number and calibration from the manufacturer and using a digital interface to the XBT bridge circuit output, the temperature-axis error could be improved to .025°C. This accuracy is comparable to the aggregate of the STDs now in use (Scarlet, 1975). The use of the potential temperature-salinity relation between 100 and 800 db in the MODE region is good to .02°/₀₀ salinity, and would introduce an 8% error in dynamic heights, sufficient to define the dynamic topography (Scarlet, MODE Hot Line News No. 57; Fofonoff, MODE Hot Line News No. 43). Also, Sippican is developing an expendable temperature-salinity probe (XSBT) with the addition of a thermistor to their expendable sound velocimeter. It is premature to estimate what the salinity resolution will be. However, between 500 and 1500 db in the MODE region systematic errors of 3.9 db in depth, .0067°/₀₀ salinity, and .029°C in temperature introduced a 5% error in dynamic height (Scarlet, private communication, 1974). It is foreseeable that an expendable bathythermograph with salinity will be available with the accuracy of the aggregate of the STDs now in use.

References

Flierl, G. and A. Robinson (1977) XBT measurements of thermal gradients in the MODE eddy. J. Phys. Oceanogr., 7(2), 300-302.

Scarlet, R. (1975) STDs in MODE -- A Grab Bag of Calibration Problems: The Results. Proceedings of the 3rd STD Conference, Plessey Environmental Systems (Suppl.).

Schlichting, H. (1955) Boundary Layer Theory. McGraw-Hill, New York.

AN EXAMPLE OF THE LAGRANGIAN MASS TRANSPORT BY FINITE AMPLITUDE ROSSBY WAVES (continued)

particle obtained for a given initial position of the particle, $\underset{\sim}{x}_o$ at t=0. For the present problem, (12) is intrinsic nonlinear, and a numerical integration is necessary to obtain the particle motion along each Q-line. The only exception is the straight constant Q-line at $y = \frac{\pi}{2L_2}, \frac{-\pi}{2L_2}$, etc. (Figure 8), where the velocity takes on a rather simple form. We will focus on the line at $y = \frac{\pi}{2L_2}$. Along this line, the fluid motion is strictly east-west, and (12) reduces to

$$dx/dt = \psi_o L_2 \sin[K_1(x+c_x t)]$$

where (4) is used. Changing the variable, $\xi' = K_1(x+c_x t)$, and integrating the above equation over one full cycle, one has

$$t = (1/K_1 c_x) \int_0^{2\pi} d\xi'/[1+(L_2\psi_o/c_x) \sin\xi']$$

$$= (2\pi/K_1)(c_x^2 - L_2^2\psi_o^2)^{-\frac{1}{2}},$$

(continued page 10)

AN EXAMPLE OF THE LAGRANGIAN MASS TRANSPORT BY FINITE AMPLITUDE ROSSBY WAVES (continued)

in which the initial condition $x = 0$ at $t = 0$ is assumed. The total distance that the particle traverses over one wave cycle is $x = (2\pi/K_1) - c_x t$. Thus, the average Lagrangian particle speed in one cycle is just

$$\frac{x}{t} = (c_x^2 - L_2^2\psi_o^2)^{+\frac{1}{2}} - c_x$$

$$= -L_2^2\psi_o^2/2c_x \quad \text{for } c_x >> L_2\psi_o \ .$$

The second result may be compared with the Stokes drift U_x obtained earlier. One can also see that for $L_2\psi_o = c_x$ the particle speed equals the phase speed.

In conclusion, the above result can be extended to three or more non-interacting Rossby waves, and more complicated patterns of the trapped mass may be constructed. The method for computing the Lagrangian motion by following the potential vorticity lines can be applied to the fully interacting Rossby wave field as well. A generalization of the method to a slightly viscous fluid also appears possible. These possibilities are being explored.

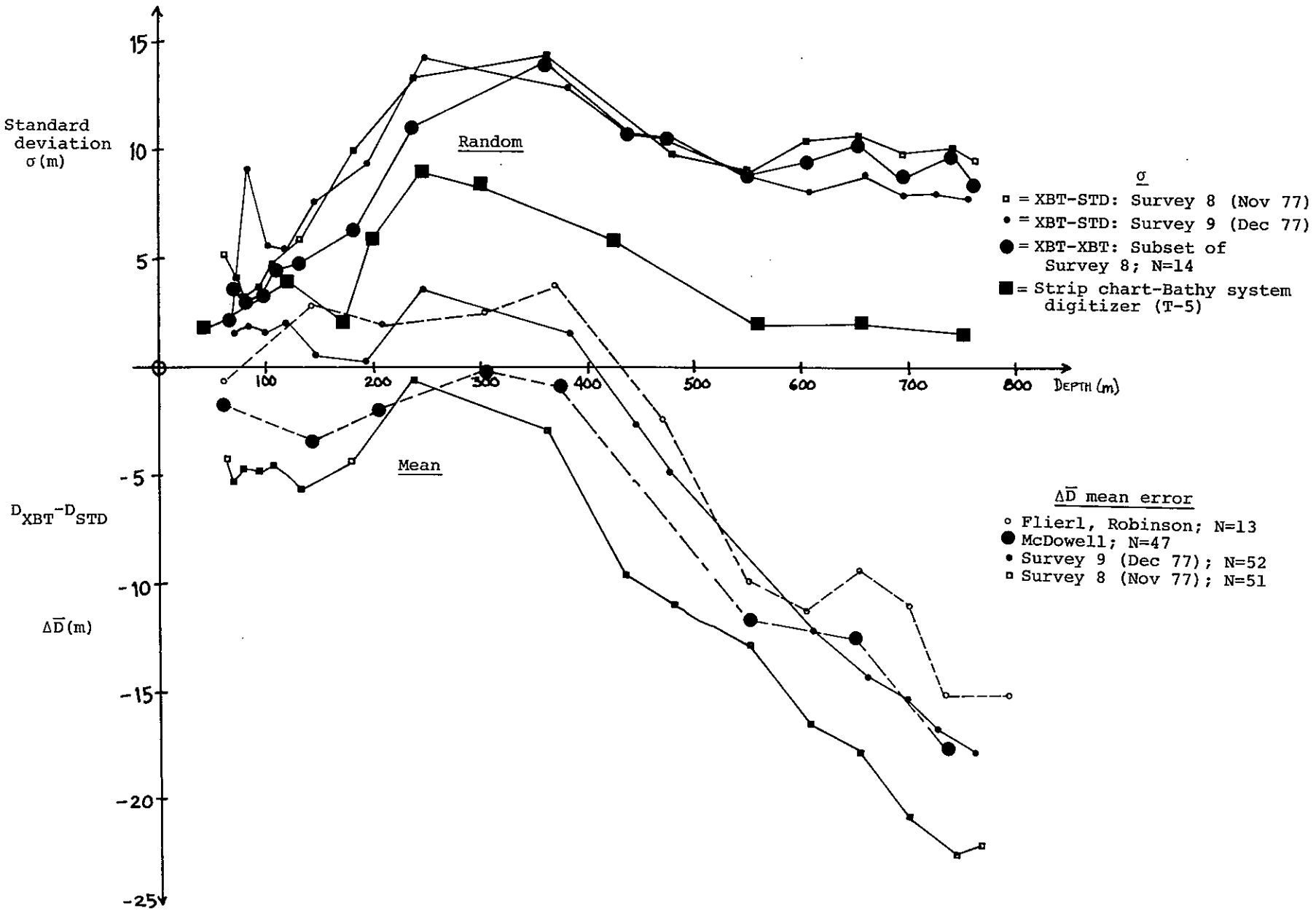

XBT depth error (mean error and the standard deviation of the random error) vs. depth.

Figure 1 (Seaver and Kuleshov)

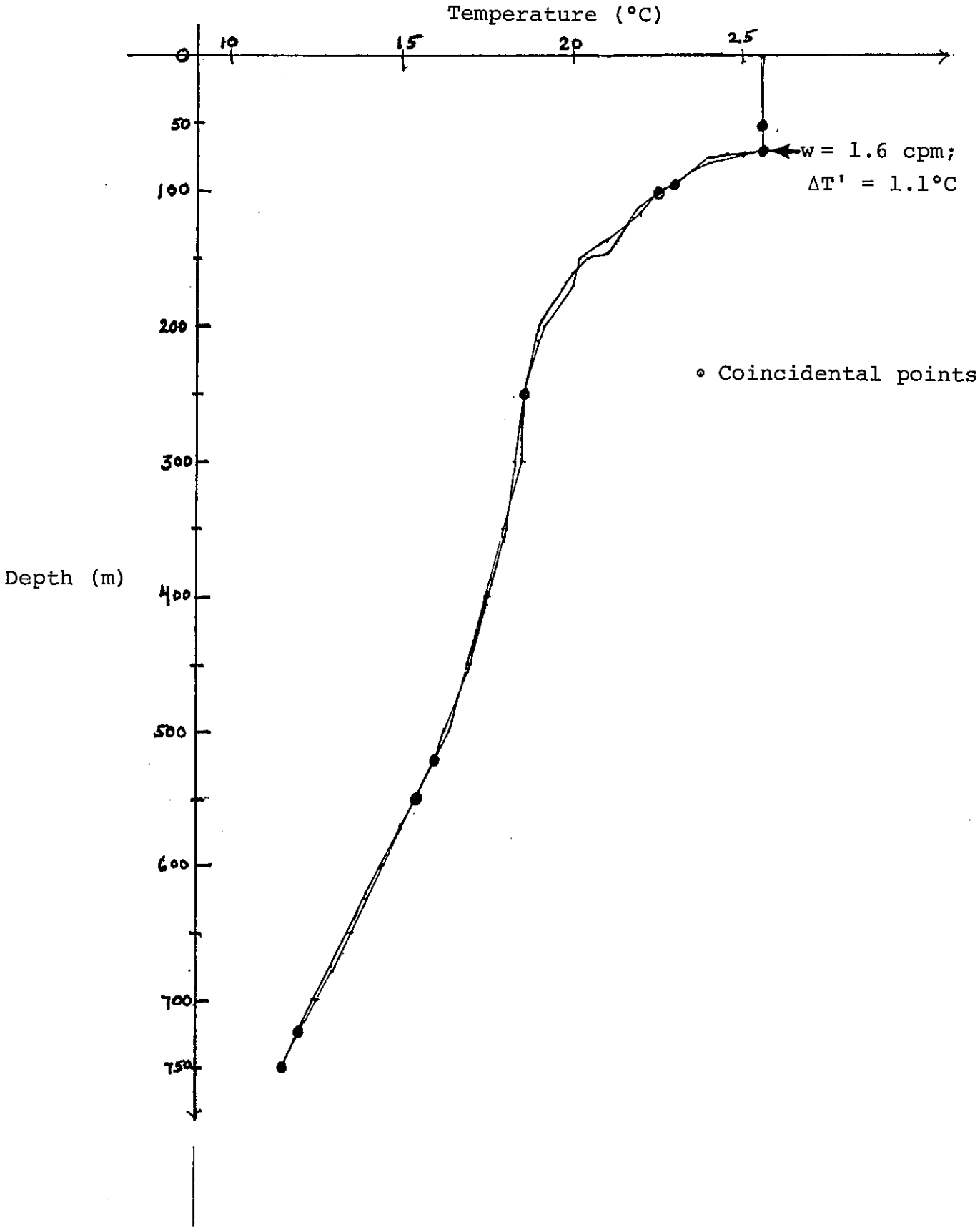

Temperature vs. depth profiles for 2 XBTs taken in the same location 66 minutes apart, at the beginning and end of an STD drop.

Figure 2 (Seaver and Kuleshov)

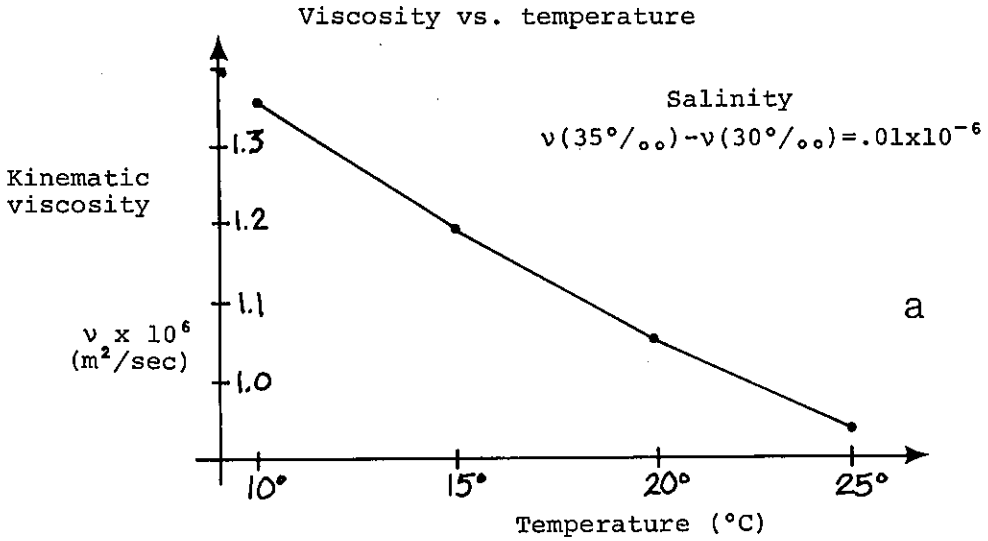

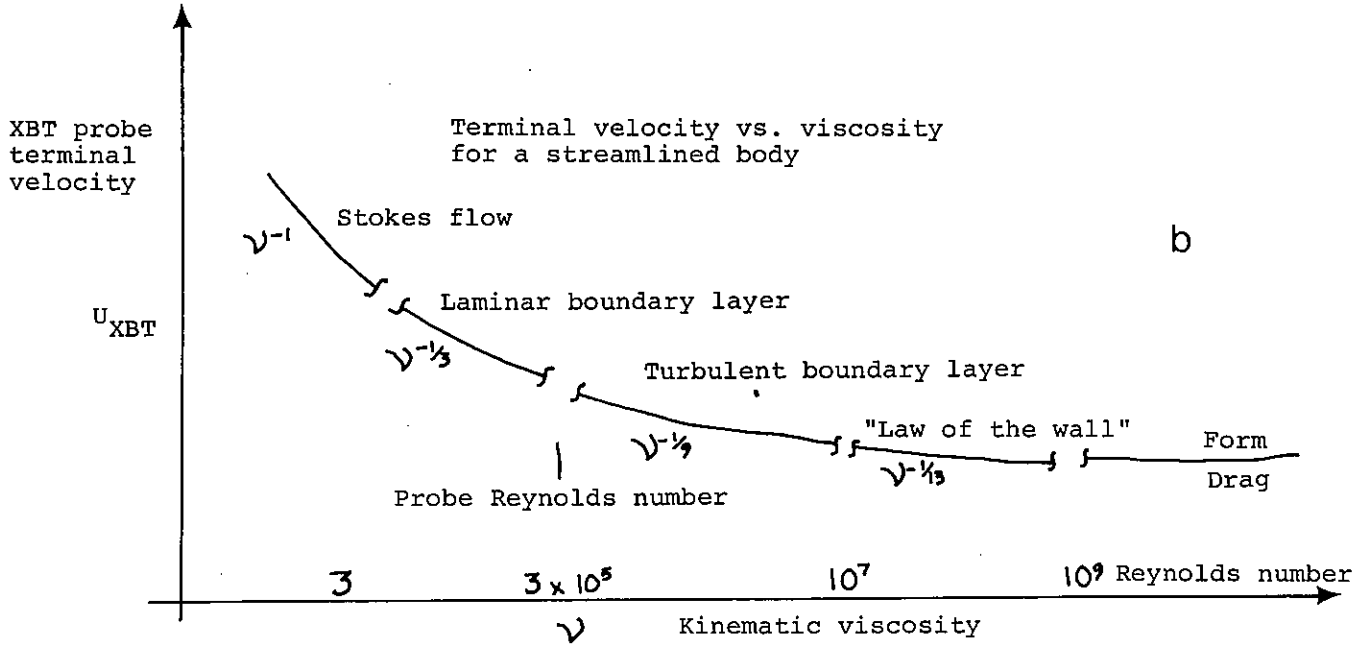

(Relative vertical positions of the curve segments not necessarily correct)

a) Kinematic viscosity vs. temperature;
b) terminal velocity vs. viscosity (from Schlichting, 1955).

Figure 3 (Seaver and Kuleshov)

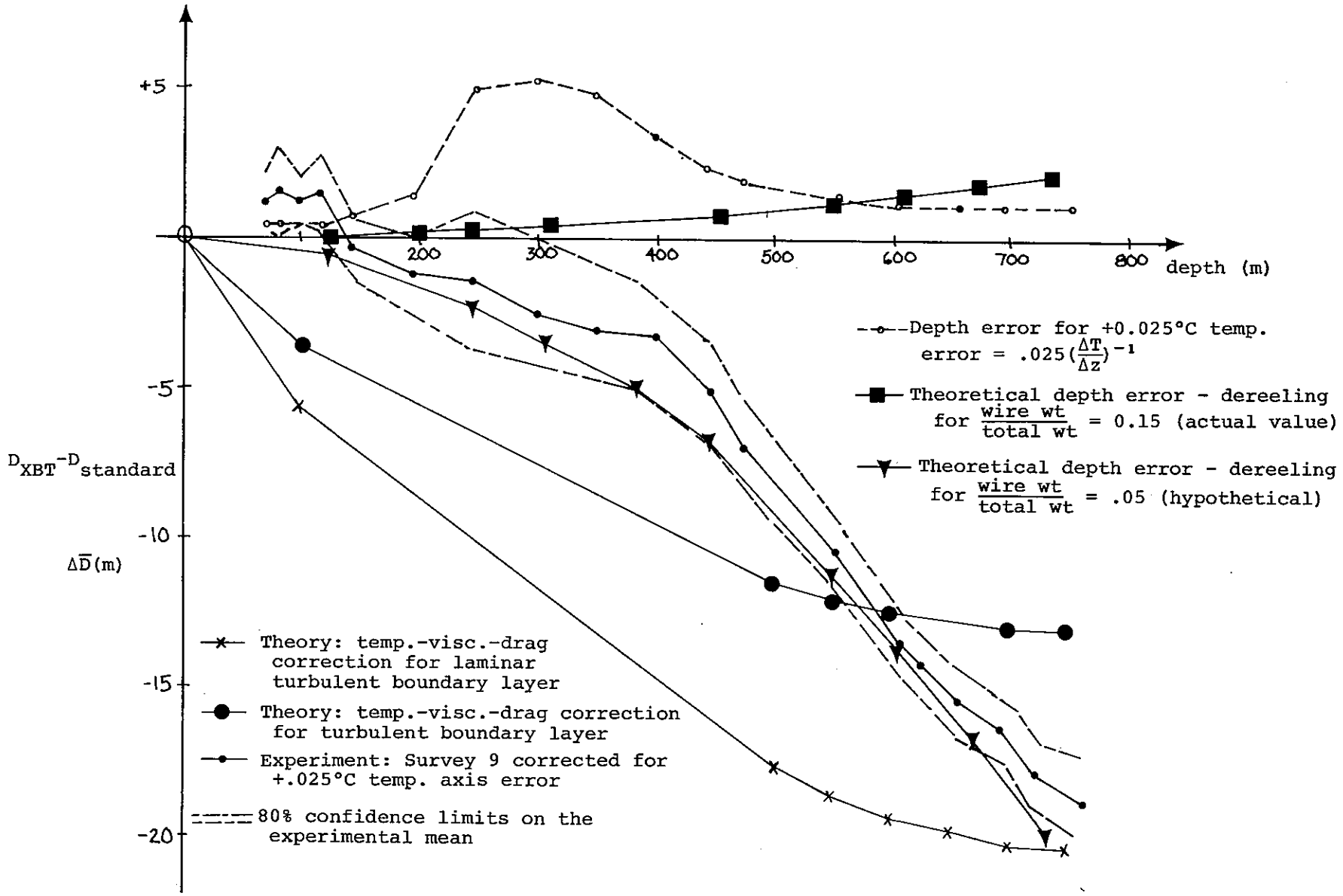

Mean depth error vs. depth from theory and experiment for the 750 m T-7 probe.

Figure 4 (Seaver and Kuleshov)

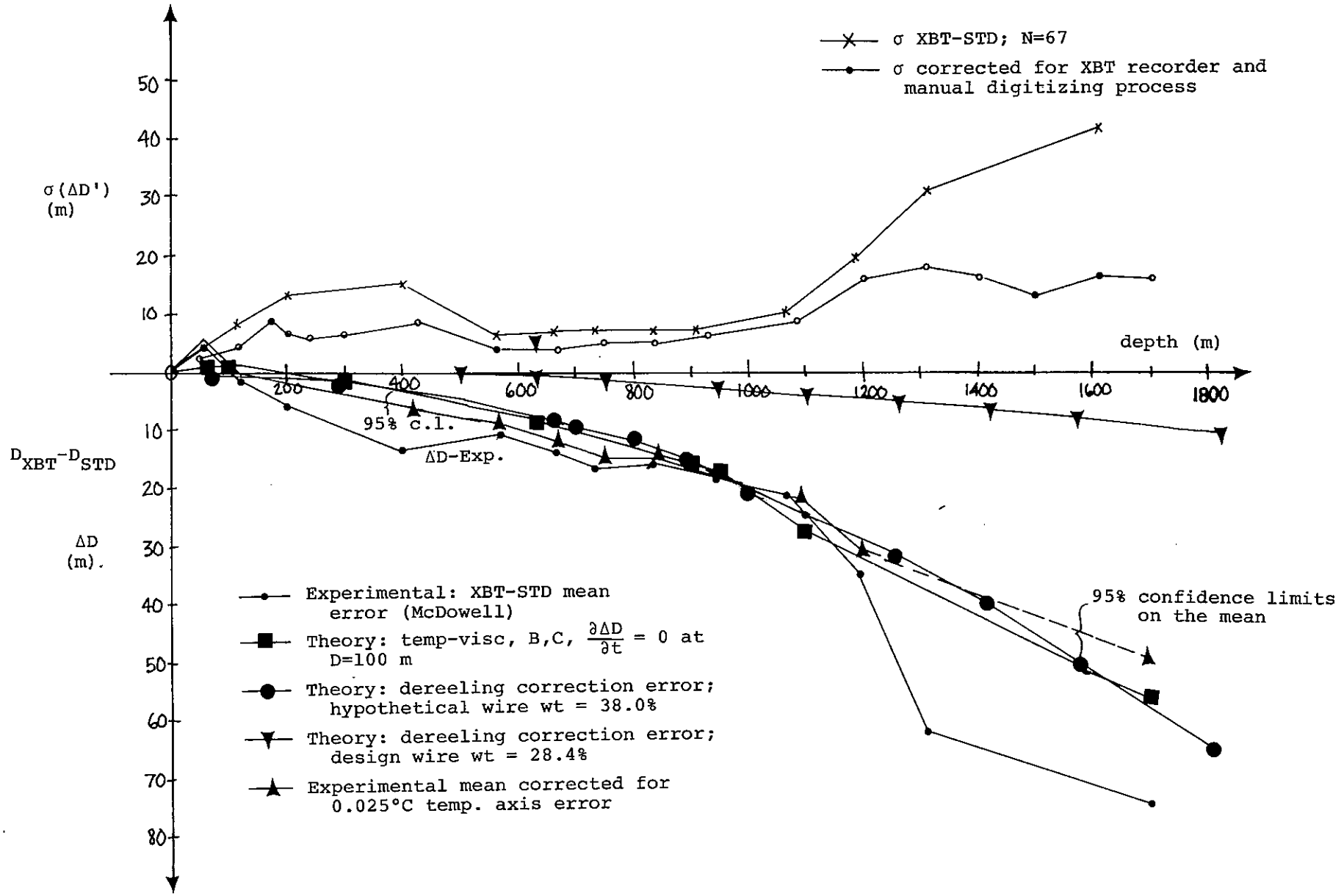

XBT depth error vs. depth for the 1800 m T-7 probe (McDowell, POLYMODE News No. 29).

Figure 5 (Seaver and Kuleshov)

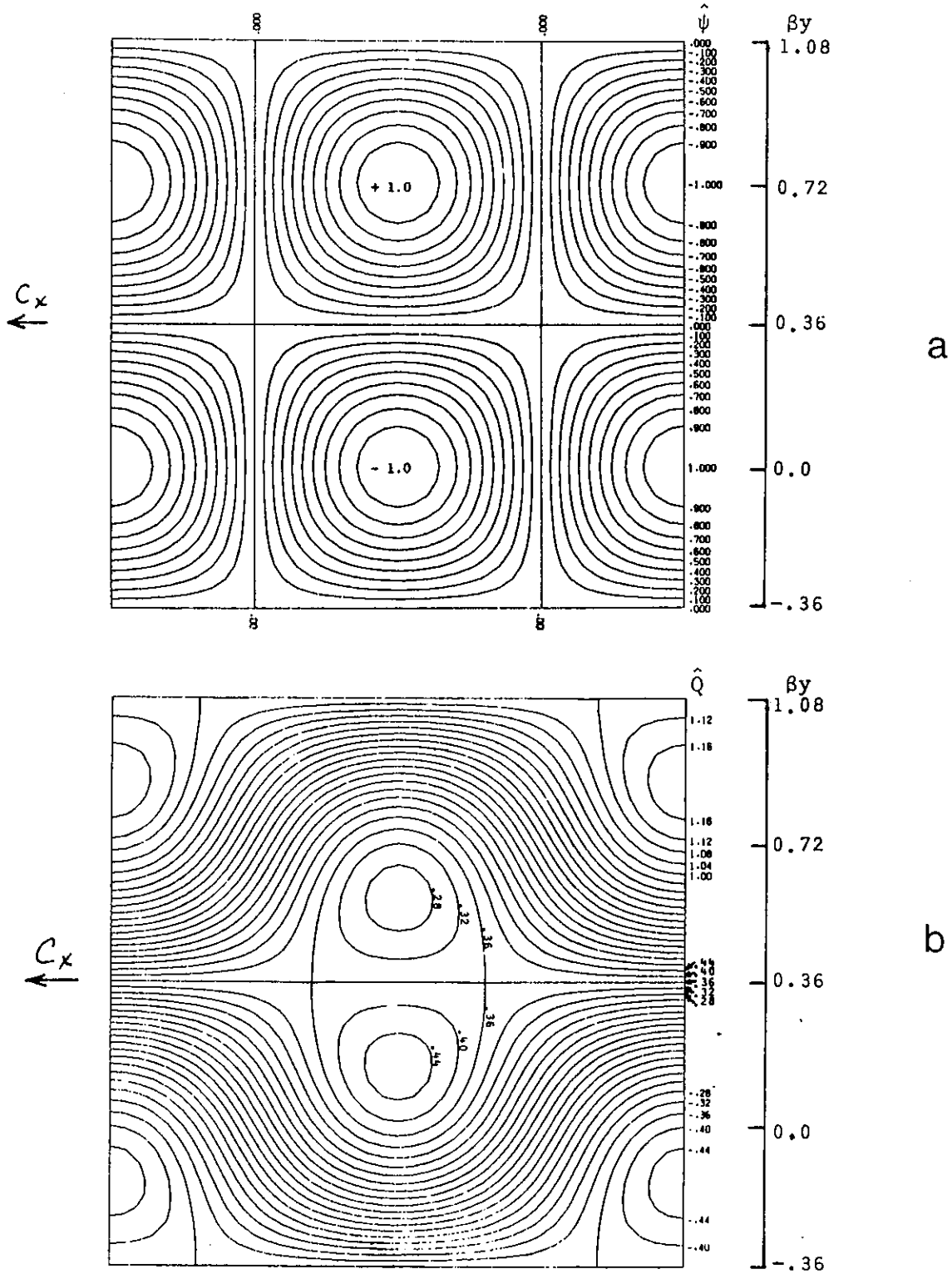

a) Streamlines and b) lines of constant potential vorticity for ψ given by equation (4) with $L_1 = 0 = K_2$ and $\psi_o > K_1 c_x/(D \sin\phi_1 \sin\phi_2)$. The areas within the enclosed contour near the center and those at the four corners in (b) represent the trapped masses; the patterns are periodic in space and move to the west. At the right side, values of streamline contours are under $\hat{\psi}$(a), potential vorticity contours are under $\hat{Q}$(b), and background planetary vorticity is under βy(a,b). All values are dimensionless and are chosen for the convenience of the presentation.

Figure 6 (Shen)

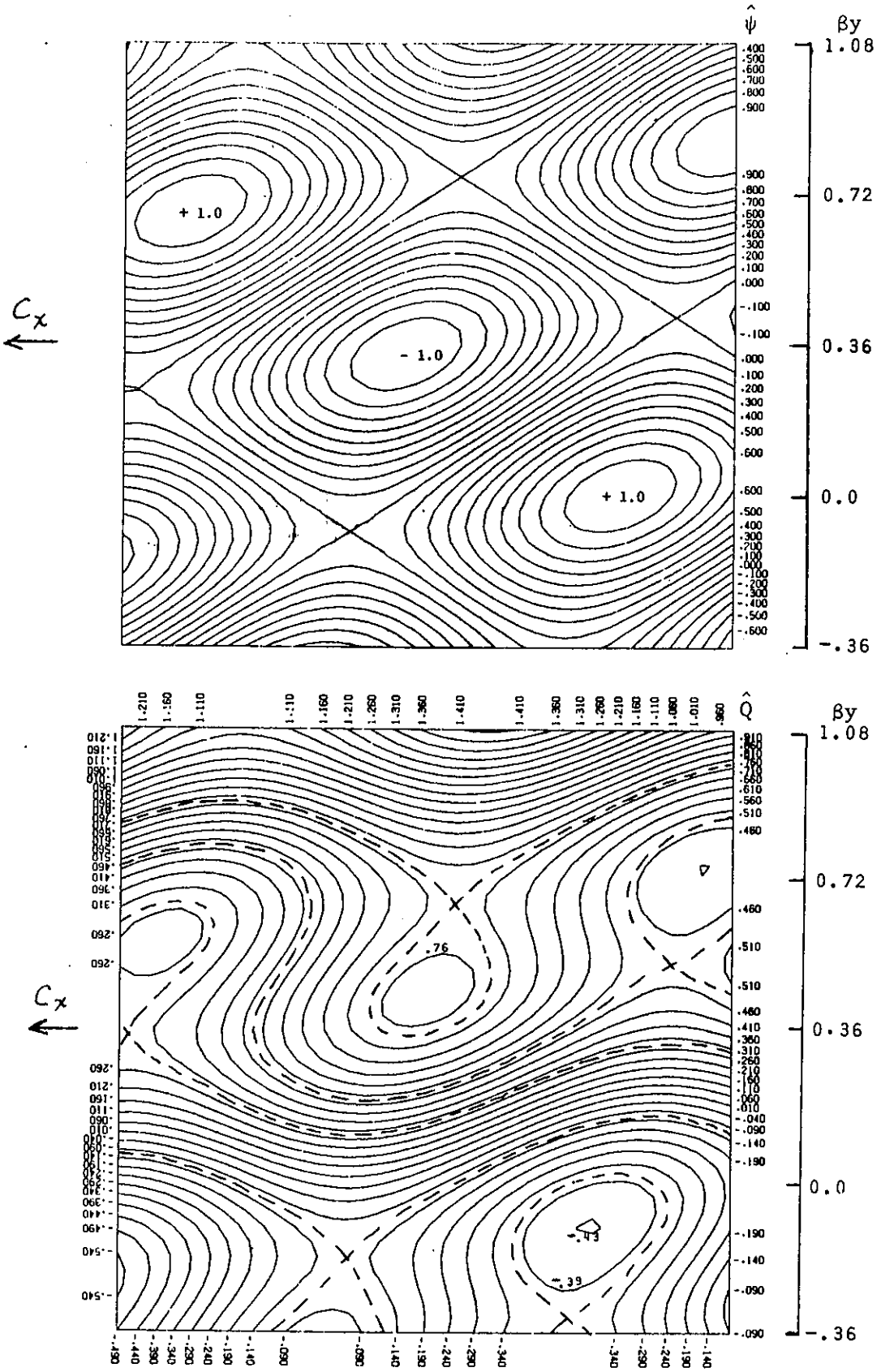

Caption same as Figure 6, except $L_1 \neq 0$ and $K_2 \neq 0$. The dash lines in (b) are hand drawn contours.

Figure 7 (Shen)

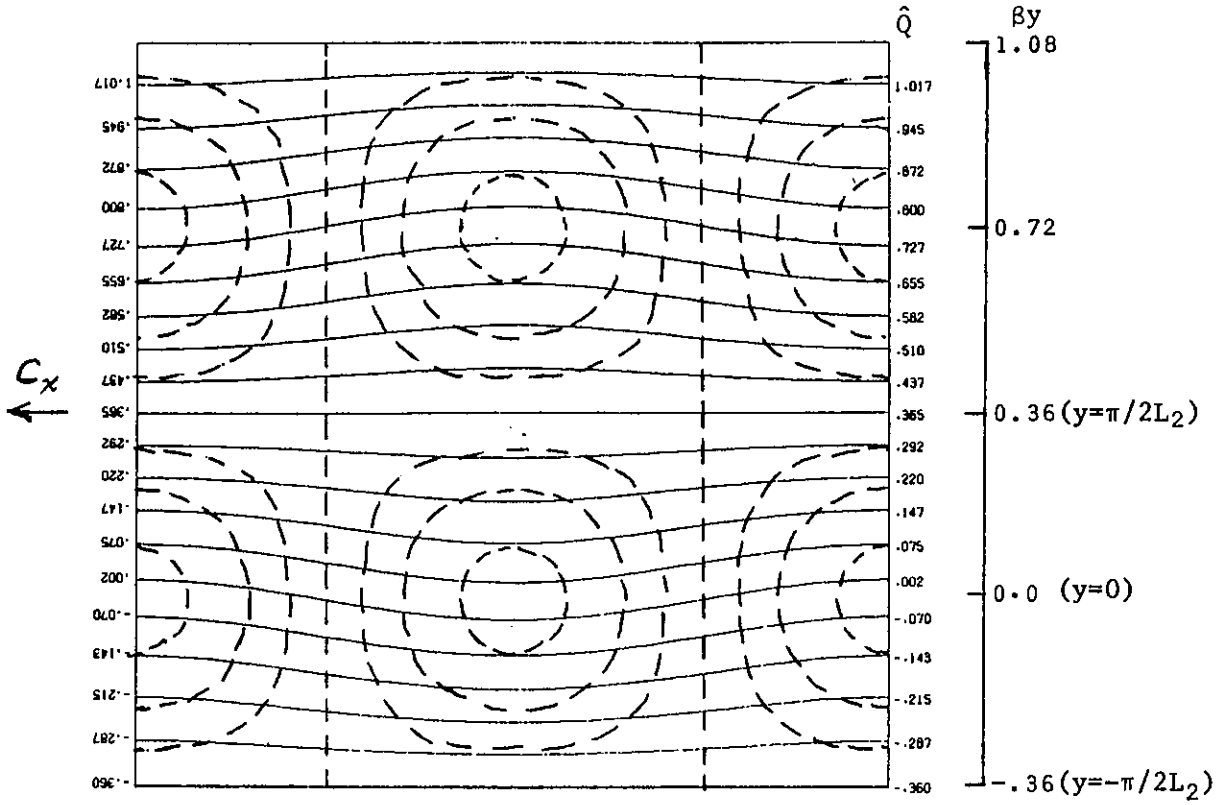

Caption same as Figure 6, except $\psi_o < K_2 c_x/D$. The dash lines are the streamlines. The solid lines are lines of constant potential vorticity.

Figure 8 (Shen)